Journal of Catalysis 433 (2024) 115483

Contents lists available at ScienceDirect

Journal of Catalysis

journal homepage: www.elsevier.com/locate/jcat

Research article

Steady-State and transient kinetic investigations of the oxidation of NO over Pt/SiO_2

Moses Mawanga, Jia Yang, Edd A. Blekkan *

Department of Chemical Engineering, Norwegian University of Science and Technology, Sem Sælands vei 4, 7491 Trondheim, Norway

ARTICLE INFO

Keywords:
NO oxidation
SSITKA
Kinetic modeling
Reaction mechanism
Langmuir-Hinshelwood kinetics
High NO concentration

ABSTRACT

The reaction mechanism of the oxidation of NO under conditions of high NO concentration over a 2 wt% Pt/SiO_2 was studied using both kinetic and transient isotopic tracing experiments. The reaction mechanism was found to involve both NO adsorption and oxygen adsorption, contrary to the situation under low NO concentration where NO reacts from the gas phase. The kinetic rate data could be fitted to the Langmuir-Hinshelwood model permitting the estimation of rate and equilibrium constants of elementary steps. These steps were investigated using transient responses following independent reactant gas isotopic switches for tracing the nitrogen path and the oxygen path during NO oxidation. These transients could be sufficiently described by a microkinetic model based on two pools of NO intermediates, one pool each for the adsorbed molecular oxygen and atomically adsorbed oxygen. Surface atomic oxygen was found to be formed by two different routes: via a direct dissociation of molecularly adsorbed oxygen and also via an assisted pathway that leads to NO_2 formation. The latter surface reaction between adsorbed NO and adsorbed molecular oxygen comprised the kinetically relevant step. Insights from the two experimental and model approaches were in good agreement and provided a coherent reaction mechanism for NO oxidation under high NO reactant concentration.

1. Introduction

The oxidation of nitric oxide to form dioxide is a very important reaction in several industrial processes. Such processes include the remediation of NO_x-containing effluent gases emitted from combustion processes and the nitric acid manufacture for fertilizer production where the oxidation of nitric oxide is an intermediary step. Furthermore, the oxidation of NO is a critical reaction in exhaust gas cleaning, e.g., from vehicles. NO oxidation involving high NO reactant concentration is an especially significant reaction in nitric acid manufacture because the effective conversion of NO to NO_2 enables the attainment of high nitric acid yields, while unoxidized NO may result in the unwanted formation of N_2O [1,2].

There are notable differences in the conditions for NO oxidation between the exhaust gas cleaning and industrial process of nitric acid production. Specifically, the concentration of NO reactant in nitric acid production can be up to 2 000 times higher compared to NO_x remediation. In NO_x remediation, the concentration of NO is typically very dilute, ranging from ten to a few hundred parts per million (or < 0.01 %), whereas in nitric acid production, NO concentrations are much higher, reaching up to 10 %. Additionally, the operating pressures differ; NO oxidation in NO_x remediation typically happens at near ambient pressures, while in nitric acid production, it ranges from medium to high pressures (3–10 bar), especially in the typical dual-pressure plants [3]. These varying conditions greatly influence the choice of catalytic system for each process.

In the production of nitric acid on an industrial scale, ammonia is combusted to produce mainly nitrogen monoxide which, when oxidized by air produces nitrogen dioxide in an uncatalyzed gas phase reaction. This reaction obeys peculiar kinetic laws, often being described as a third-order reaction with a negative activation energy over a wide temperature range (from sub-ambient temperatures up to around 375 °C)[4]. At high temperatures, the homogeneous oxidation reaction, albeit occurring spontaneously, does so at very slow rates thus necessitating cooling the gas to ambient temperature and allowing enough time for the reaction to reach completion. Effluent gases from the ammonia burner need to be cooled down drastically and allowed sufficient residence time to achieve economically acceptable degrees of oxidation. Alternatively, oxidation rates can be enhanced by introduction of a heterogeneous catalytic reactor operating at high temperature and pressure such that the long residence time and cooling requirements

* Corresponding author.
E-mail address: edd.a.blekkan@ntnu.no (E.A. Blekkan).

https://doi.org/10.1016/j.jcat.2024.115483
Received 29 January 2024; Received in revised form 26 March 2024; Accepted 6 April 2024
Available online 9 April 2024

Nomenclature

Symbols and abbreviations

E_a	Apparent activation energy
k_i	Rate constant of step i
K_i or K_{eq}	Equilibrium constant of step i
B_o	Bodenstein number
U	interstitial gas velocity (m/s)
ρ_b	Density of catalyst (kg/m^3)
ε_b	Void fraction of the catalyst
θ_i	Surface concentration of intermediate species i (mol kg^{-1})
τ	Hydraulic residence time (s)
SSR	Sum of squares residuals
MASI	Most abundant surface intermediate
DOC	Diesel oxidation catalyst
XRF	X-ray fluorescence

may be excluded from future nitric acid production processes. The improved and compact catalytic process for NO oxidation is proposed to have a major advantage of a reduced plant size and a more efficient energy recovery [5].

Metals such as Pt and Ru, as well as oxides like MnO_x, can potentially serve as catalysts for the high concentration NO oxidation reaction relevant to nitric acid production. Grande et al. examined the kinetics of NO oxidation over Pt/Al_2O_3 as an initial catalyst assessment for intensifying the NO oxidation process [5]. A reactant feed containing 0.25–5 % NO, 1–8 % O_2, and 0–20 % H_2O was used in studying NO oxidation kinetics between 250 and 350 °C. Their research work demonstrated the potential of Pt in oxidizing NO under humid conditions typical of nitric acid production. Salman et al. expanded on the study of Pt, highlighting that the rate of NO oxidation over 1 wt% Pt/Al_2O_3 remained independent of NO concentration but observed a fractional-order dependence on O_2 concentration in a dry feed with 5–11 % NO and 3–9 % O_2 at 300 °C [6]. A Langmuir-Hinshelwood Hougen-Watson reaction mechanism was proposed, considering the desorption of NO_2* as the kinetically-relevant step. However, the strong and ubiquitous inhibition of the rate of NO oxidation by product NO_2 renders the desorption of NO_2 being rate-determining unlikely. Recent reports have also explored the kinetics of NO oxidation under high NO concentrations over non-platinum catalysts. Catalysts such as Ru/Al_2O_3 [7] and $MnO_2/Ag/ZrO_2$ [8] have the potential to catalyze NO oxidation under conditions resembling nitric acid production even at a pressure of 4 bar.

Supported platinum metal is known to catalyze NO oxidation under conditions of low NO reactant concentration [9–13], in levels of ppm due to its innate catalytic oxidation capability. The remediation of low NO concentrations to environmentally benign N_2 via Selective Catalytic Reduction (SCR) is used in industrial gas cleaning processes and in diesel exhaust engines. The exhaust gas is contacted with a diesel oxidation catalyst, DOC, in which the platinum component converts NO into NO_2 and finally into N_2 through reaction with a reducing agent such as NH_3 [14]. In an effort to understand the conversion of NO to NO_2 over Pt, the catalytic reaction has been explained via two competing plausible mechanisms, one more popular in literature than the other [15,16]. The first mechanism postulates adsorption and activation of oxygen on free Pt site followed by reaction of active oxygen species with NO from the gas-phase in an Eley-Rideal fashion. In the alternative mechanism, both oxygen and nitric oxide adsorb simultaneously and compete for the same type of adsorption sites. Subsequently, adsorbed NO and activated oxygen species undergo a surface reaction forming adsorbed NO_2 species which desorb from the surface liberating free sites to complete the catalytic cycle (i.e. a Langmuir Hinshelwood mechanism). Most studies addressing NO oxidation have dealt in the realm of low NO concentrations for exhaust gas cleaning. The same mechanisms may or may not hold for the oxidation of high NO concentrations that prevail under conditions of nitric acid manufacture.

The goal of this investigation is to study the reaction mechanism of NO oxidation over Pt/SiO_2 under conditions of high NO reactant concentration and provide insights into the various aspects of the catalytic process. To achieve this goal, we have combined both steady-state kinetic experimentation and modeling and transient isotopic tracing i.e., steady-state isotopic transient kinetic analysis (SSITKA). The method of inquiry combines conventional kinetic studies and the SSITKA approach to investigate the underlying reaction mechanism. For mechanistic studies that employ SSITKA, the reaction is allowed to reach steady state in which all the flow rates, temperature, pressure, and production rates are constant. After attaining steady state, the isotopic composition of one of the reactants is abruptly switched to its heavier isotope but maintaining the overall chemical composition. In the absence of kinetic isotope effects, important insights on the reaction mechanism can be gleaned from the appearance of the isotopically labeled product and/or decay of the unlabeled product molecules.

The SSITKA technique is useful and powerful in capturing the kinetics and providing insights into the reaction mechanism [17]. Recent reviews of the SSITKA technique give a comprehensive overview of catalytic reactions that have been studied [17–21] and a few notable examples can be briefly mentioned. The Fischer-Tropsch mechanism for methane and C–C formation has been extensively studied using SSITKA modeling combined with DFT and kinetic isotope effect studies [22]. In this study, the mechanism for CO activation via a H-assisted pathway for CO dissociation was proposed being more probable than the direct CO dissociation route. In another study, Costa et al. used ^{15}NO-SSITKA combined with diffuse reflectance infra-red spectroscopy to demonstrate the nitrogen pathway during reduction of NO under lean conditions over Pt supported catalysts. The formation of both N_2 and N_2O was demonstrated to occur via two structurally different NO_x adsorbed intermediates where the surface concentration of NO_x intermediates (as determined by SSITKA) depended on the chemical nature of the support i.e., SiO_2 versus La-Ce-Mn-O. In the same study, a separate $^{18}O_2$ switch in the reactant stream showed NO_2 being an intermediate for N_2O formation and this could explain the substantial N_2O formation on Pt/SiO_2 in comparison to Pt/La-Ce-Mn-O [23]. Indeed, the high selectivity toward N_2 formation is related to surface concentration of certain N_2-forming intermediates (probed by SSITKA) which may be enhanced by addition of promoters such as Na and Mo to supported Pt catalyst. These promoters enhance the retention of nitrogen forming precursors leading to a larger delay in the N_2 transient in comparison to the unpromoted catalyst [24]. In another interesting example, the mechanism of toluene acetoxylation catalyzed by supported Palladium has been studied by SSITKA [25]. Transient kinetic analysis demonstrated that despite both lattice oxygen and adsorbed oxygen contributing to the activation of the reactant acetic acid, it was the latter that promotes the oxidation of acetic acid to undesired CO_2. These examples highlight the importance of SSITKA as a valuable tool for the kinetic study of gas solid reactions.

Isotopic transient responses of reactant and product concentration signals coupled with a modeling approach contain mechanistic information about the reaction under study, and through the modeling of transient responses underlying mechanistic information can be obtained. Analysis of the of isotopic relaxation spectra and isotope label transfer provides information on the underlying mechanism of the reaction under consideration. The shape of the response curve in logarithmic scale provides preliminary insights into the mechanism. The logarithmic plot of molar flow rates versus time demonstrates specific features of the isotopic response for a given mechanism. Sadovskaya et al. [26] posits that the plot may be linear for a one pool mechanism. For a two-pool mechanism, the plot has an upward convexity whereas a downward convexity signifies a mechanism involving parallel or buffer steps. In the latter case, these two models can be discriminated

exclusively on the basis of numerical analysis and curve fitting of the observed isotopic transients to extract mechanistic information. Therefore, isotopic tracing and modeling is a useful kinetic tool for studying mechanisms of surface-catalyzed reactions.

2. Experimental details

2.1. Catalyst preparation and characterization

Silica supported Pt catalysts were prepared by dry impregnation. Silica was selected because unlike other supports like Al_2O_3 and ZrO_2, it does not retain NO_x [27]. This attribute of SiO_2 is important for SSITKA which works on the principle of intermediate retention on the catalytic surface, thereby eliminating artifacts that may be caused by support retention effects. Silicon dioxide (Davisil grade, Sigma-Aldrich) was heated at 10 °C min^{-1} to 400 °C and kept at this temperature for 4 h. Hexachloroplatinic acid hexahydrate ($H_2PtCl_6{\cdot}6H_2O$, Merck KGA) was dissolved in distilled water and the solution was added to SiO_2 until an incipient wetness point was reached (0.75 $cm^3/gSiO_2$). One set of impregnated supports were dried in air at 120 °C for 4 h and calcined in flowing air at 600 °C. Another batch of the same dried impregnated sample was calcined for 1 h at 150 °C in a stream of 7.5 % hydrogen flow. The sample was sieved to retain a size range of 150–200 μm. Elemental analysis of the two catalysts with X-Ray Fluorescence, XRF showed ~2.2 wt% loading of Pt. Details of catalyst characterization for N_2 physisorption, X-Ray diffraction, H_2 chemisorption, and STEM-EDX are included in section S1 of the supplementary information.

2.2. Catalytic testing

The catalysts were tested for NO oxidation activity under conditions that mimic industrial conditions for nitric acid production: 5 % NO, 6 % O_2, and inert within a relevant temperature range of 280–350 °C. High pressure experiments were not possible in this study and thus all experiments were conducted at 185 kPa pressure. The reactor setup was used for both kinetic and SSITKA experiments. A U-shaped quartz reactor with 4 mm inlet ID and a narrower exit ID was purposely built to minimize the reactor dead volume. The catalyst sample was held between two quartz wool plugs. Reactant gases 40 % NO/Ar, 40 % O_2/Ar (BOC), and Argon (AGA, 99.999 %) were metered using mass flow controllers (Bronkhorst High-Tech B.V.) to achieve different ranges of reactant pressure for steady state reaction rate experiments. The temperature of the reactor was controlled using a resistively-heated furnace and a K-type thermocouple (located inside the catalyst bed) to achieve constant temperature measurements. The reactor inlet and outlet gas concentrations were measured using an online quadruple mass spectrometer (QMG 422, Pfeiffer) fitted with a yttriated iridium filament suitable for use in highly oxidizing atmosphere (see also section S2 of the supplementary information).

Temperature-programmed surface reaction experiments were performed to ascertain the optimum level of NO conversion well above the gas phase NO oxidation level. The profile of NO conversion was followed with a linearly increasing temperature and thus showed the temperatures at which SSITKA experiments would be performed to discern the catalytic contribution to the reaction above that of the gas phase. During the experiments, the reactor temperature was increased at 3 °C min^{-1} from 100 to 450 °C. For the kinetic experiments, a sample of Pt/SiO_2 (Pt loading: 2.2 wt%, 0.145 g, particle size: 150–250 μm, catalyst bed height: 3 cm) was heated to 450 °C in a stream of 7.5 % H_2 for 1 h and cooled to 330 °C in an argon flow. The reactor was held at 330 °C and then exposed to the standard reactant feed (5 % NO, 6 % O_2, and Ar balance or 9.3 kPa NO, 11.1 kPa O_2, and 164.6 kPa Ar). After attaining steady state, the reactant composition was changed in a random fashion to give a range of NO oxidation rates as a function of reactant pressures. The same kinetic experiment was repeated at 303 and 280 °C using a fresh catalyst sample for each of these experiments. Figs. 2 and 3 include repeated experiments indicating the absence of detectable deactivation during the experimental run.

Initially, an empty reactor had been used to quantify gas phase conversion but sustenance of stable MS signals with back pressure regulation proved difficult with a mere void. Therefore the testing protocol to quantify the gas phase conversion in the absence of a catalyst was performed using catalytically inert silicon carbide (non-porous, particle size 150–250 μm).

2.3. Transient kinetic catalytic testing

2.3.1. Steady-State isotopic transient kinetic analysis

Each set of SSITKA experiments were performed with a fresh sample of catalyst. Typically, 0.145 g of catalyst (particle size: 150–250 μm, catalyst bed height: 3 cm) without catalyst dilution were reduced by treatment in a stream of H_2 as described in steady state experiments and cooled down to 330 °C in a stream of Ar. The unlabeled gas lines were connected to 40 % NO/Ar, 40 % O_2/Ar (BOC) and Ar (99.999 % AGA). The isotopic gas line was connected to ^{15}NO (99 %, BOC), $^{18}O_2$ (97.15 atom %, Euroisotope) and Krypton (99.999 % AGA). For switching between gas streams, a 4-way valve was used whose response was much faster than the response of the catalytic system being measured. The influence of the dead volume of the valves could be neglected. The schematic of the reactor setup is presented in section S2 of the supplementary information. Analysis of isotopic transient responses for the NO oxidation reaction was achieved by first running the reaction under an unlabeled reactant stream until a steady state was established. The reactant stream was then switched to labeled gas in two following ways. In the first case, the switch $^{14}NO/O_2/Ar$ // $^{15}NO/O_2/Kr = 5/6/89$ mol% was performed to investigate the nitrogen path in the mechanism of NO_2 formation. In a separate experiment using a fresh reduced catalyst, another switch $NO/^{16}O_2/Ar$ // $NO/^{18}O_2/Kr = 5/6/89$ mol% was made for tracing of the oxygen path permitting the investigation of the role of oxygen activation on the reaction mechanism.

2.3.2. Numerical modelling and kinetic parameter estimation

The SSITKA experiments were performed under non-differential reactor conditions, and thus the concentration profiles along the catalyst bed were considered. A plug flow reactor model was appropriate to describe the trend of the isotopic transients to extract kinetic parameters of NO oxidation over the surface. Consequently, a reactor model described by Berger et al. [28] was applied to evaluate the observed transient data for the separate switch experiments. Unlike the CSTR which is modeled on the basis of a differential equation in time, the PFR model introduces spatial derivative resulting in a set of partial differential equations in time and space that can be presented by Eq. 2.1-Eq. 2.4.

$$\frac{\partial C_{i^*}}{\partial t} = -\frac{1}{\tau}\frac{\partial C_{i^*}}{\partial z} + \frac{1}{\tau B_o}\frac{\partial^2 C_{i^*}}{\partial z^2} + \frac{\rho_b}{\epsilon_b}\sum\nolimits_j \nu_{ij} r_j \tag{2.1}$$

$$\frac{\partial \theta_{i^*,s}}{\partial t} = \sum\nolimits_j \nu_{ij} r_j \tag{2.2}$$

The initial and boundary conditions in an open reactor where there is continuity of flux at the boundaries at $z = L$ are at:

$$t = 0, C_{i^*} = 0, 0 \le z \le L \tag{2.3}$$

$$C_{i^*}|_{z=0} = 0, \frac{\partial C_{i^*}}{\partial z}|_{z=L} = 0 \tag{2.4}$$

where τ is the hydrodynamic residence time (s), B_o is the Bodenstein number, UL/D_{ax} (−), D_{ax} is the axial dispersion coefficient ($m^2{\cdot}s^{-1}$), ρ_b is the catalyst bulk density ($kg{\cdot}m^{-3}$), ϵ_b is the void fraction of catalyst bed (−), ν_{ij} is the stoichiometric coefficient, r_j is the reaction rate (mol_{NO} $(g{\cdot}s)^{-1}$), and $\theta_{i^*,s}$ is the surface concentration of reaction intermediate

(mol g.cat^{-1}) while C_{i^*} is the molar concentration of an isotopically labeled product (mol·m^{-3}). U and L are the average interstitial velocity and the length of the catalyst bed in $m^3_{gas}(m^2_{reactor}\cdot s)^{-1}$ and m, respectively. The determination of τ and B_o are described in section S4 of the supplementary information.

The system of partial differential equations was solved simultaneously by discretization in space along the reactor's length. Discretization was done using finite difference approximation of a variable order based on the conventional method of lines [29]. Time integration of the discretized set of equations was performed using the ode15s function within a Matlab package. Afterwards, a Levenberg – Marquardt algorithm was applied to fit the model to the experimental data using the sum of squares of residuals as the objective function until a local minimum was found.

$$SSR = \sum_{n=1}^{N_c} \left(y_n^{exp} - y_n^{calc}\right)^2 \tag{2.5}$$

Where SSR is the sum of square residual between the calculated and experimental values, representing the objective function, n is the number of partial differential equations or the number of data points, whereas y^{exp} and y^{calc} respectively are the experimental and the iteratively calculated values.

3. Results and discussion

3.1. Temperature-programmed reaction

Fig. 1 shows the variation of conversion of NO to NO_2 with temperature over SiC and also over Pt/SiO_2 catalysts calcined under different conditions. The feed comprised of 9.3 kPa NO, 11.1 kPa O_2, and 164.6 kPa Ar corresponding to 5 mol% NO, 6 mol% O_2, and 89 mol% Ar. The NO conversion over SiC represents contribution from the gas phase oxidation whereas the conversion obtained with the catalyst corresponds to the total conversion of both catalytic and gas phase contributions. Some physical characteristics of the catalyst and NO oxidation performance of the Pt/SiO_2 pretreated under different conditions are shown in Table 1.

The turnover frequency was calculated based on the number of chemisorption sites Pt from the equation.

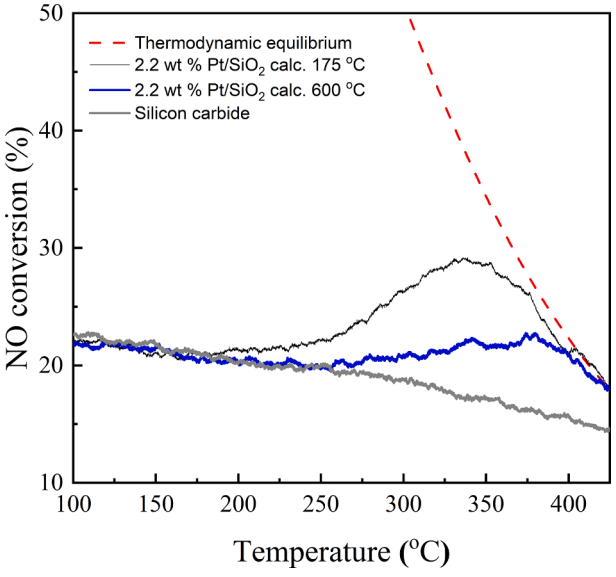

Fig. 1. Temperature-programmed reaction for NO oxidation for Pt/SiO_2 catalysts pretreated under different conditions. Reaction conditions: Feed: 5 mol% NO, 6 mol% O_2, and 89 mol% Ar, 185 kPa, 20 690 Ncm^3 g^{-1}h^{-1}.

$$TOF = \frac{rM_{Pt}}{x_{Pt}D} \tag{3.1}$$

With r being the reaction rate, mol$(g_{cat}\cdot s)^{-1}$, M_{Pt}, x_{Pt}, and D are the atomic weight, weight fraction of Pt in the catalyst and the metal dispersion respectively.

As seen in Fig. 1 the two catalysts exhibit different NO conversion profiles. Pt/SiO_2-175 lights-off at ~ 175 °C and the NO conversion increases with temperature to a maximum (29.5 %) at 330 °C. Pt/SiO_2-600 is clearly less active, has a higher light-off temperature and reaches maximum conversion at a higher temperature. In contrast to the catalytic results, the gas phase conversion using SiC decreases steadily within the test temperature range. The point of maximum conversion observed at 330 °C with Pt/SiO_2-175 coincides with 17.5 % conversion for the gas phase contribution. The homogeneous contribution can be accounted for to estimate the conversion attributable only to the catalyst in all experiments. Moving forward, Pt/SiO_2-175 was chosen for further experiments because it gave a better resolution and a higher difference between the catalytic and the homogeneous conversions at the relevant temperature.

3.2. Effect of reactant pressure on NO oxidation reaction rate

Reaction rates for NO oxidation were measured over SiC and 2.2 wt% Pt/SiO_2 using feed comprising 3.7–18.5 kPa NO (2–10 mol%), 7.4–17.6 kPa O_2 (4–9.5 mol%), and Ar. Temperature and total pressure were constantly maintained at either 330, 303, or 280 °C and 185 kPa, respectively. At these reaction conditions, for all data points, the approach to equilibrium factor i.e., β was negligible to the observed NO conversion levels. This factor ranging between 0.002–0.007 meant that the observed rate was far away from equilibrium. The gas phase contribution was accounted for by subtracting gas phase conversion from total conversion. Fig. 2 shows the variation of the catalytic NO oxidation reaction rate as a function of NO pressure and that the NO oxidation rate increases exponentially with NO pressure. Fig. 3 shows the variation of the catalytic NO oxidation reaction rate as a function of O_2 pressure in which the catalytic oxidation rate increases rather logarithmically with O_2 pressure.

3.2.1. Kinetic models for Pt-catalyzed NO oxidation

Kinetic expressions derived from sequences of elementary reactions can reliably be used to quantitatively describe observed kinetic trends due to reactant pressure effects. There are two prevailing reaction mechanisms suggested for NO oxidation over Pt catalysts, namely the Eley-Rideal and the Langmuir-Hinshelwood mechanisms. For the investigation of the reaction mechanism under these conditions, both reaction mechanisms are considered for kinetic modeling using several subcases involving different rate-determining steps, different quasi-equilibrated steps, and MASI assumptions. The scheme based on Eley-Rideal mechanism (shown in Scheme 1) is a popular reaction mechanism, frequently regarded in literature to describe and predict NO oxidation kinetics for low NO reactant pressure [9,11,12,15,30,31]. In this scheme, oxygen gas molecularly and reversibly adsorbs onto a free Pt site (*, step 1a) and dissociates on another neighboring site to form chemisorbed oxygen (O*, step 1b). As far as oxygen adsorption is concerned, theoretical studies have shown that O_2 activation dissociation on Pt always proceeds via a molecularly adsorbed precursor state [32] before forming atomic (chemisorbed) oxygen. Chemisorbed oxygen is also formed by reaction of molecularly adsorbed oxygen with NO from the gas phase (step 1c). The formed atomically adsorbed oxygen may react with NO to form NO_2 in a subsequent step (step 1d). The desorption of NO_2 (step 1e) is assumed to be fast and quasi-equilibrated, completing the catalytic cycle. Rate expression for the overall reaction in which different assumptions for the RDSs are presented in Table 2. Thus, the variation of reaction rate with reactant pressure can be used to

Table 1
Surface area, metal dispersion, NO oxidation conversion, and TOF for two Pt catalysts pre-treated under different conditions.

Support/ Catalyst	Specific surface area ($m^2\ g^{-1}$)	Pore volume ($cm^3\ g^{-1}$)	Pt-dispersion (–)	H_2 uptake ($\mu mol\ H_2/g_{cat}$)	NO conversion at 330 °C	T for max. NO Conversion (°C)	TOF at 330 °C (s^{-1})
Dried SiO_2	499	0.92	–	–	–	–	–
Pt/SiO_2-175	444	0.79	0.132	7.5	0.295	330	0.43
Pt/SiO_2-600	486	0.88	0.083	4.6	0.214	375	0.49

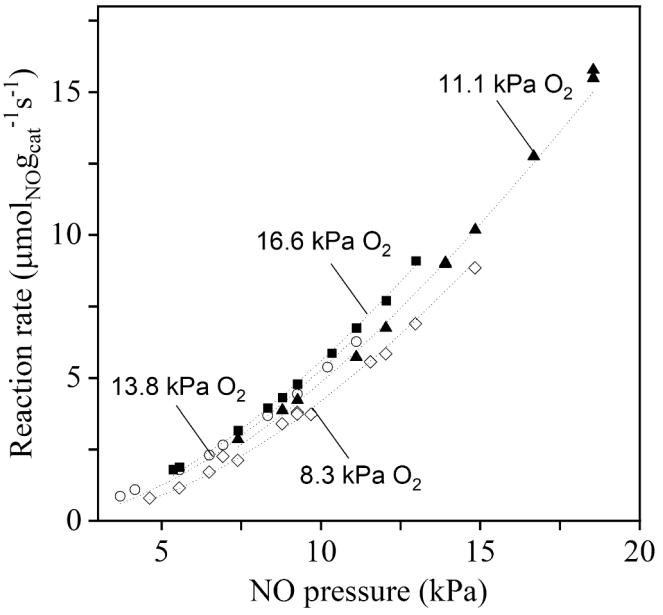

Fig. 2. Effect of NO pressure on the NO oxidation reaction rate on Pt/SiO_2 at 330 °C. The dotted lines represent the prediction of kinetic model with a rate expression presented by Eq. 3.1.

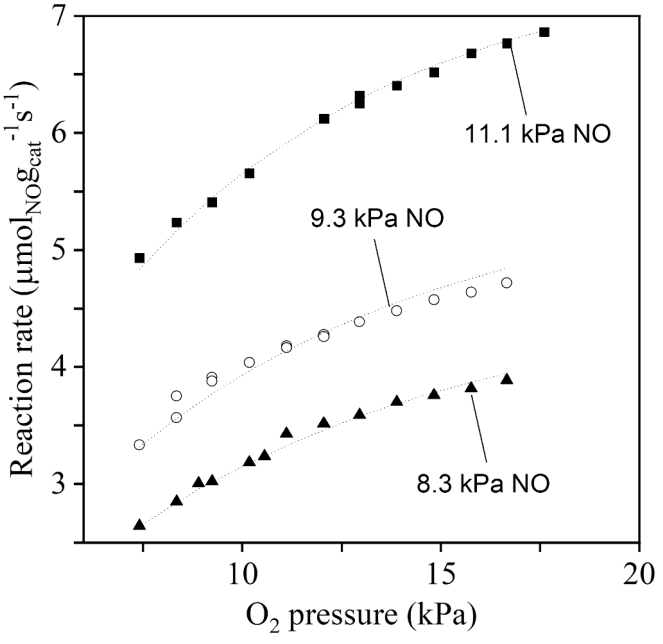

Fig. 3. Effect of O_2 pressure on the NO oxidation reaction rate on Pt/SiO_2 at 185 kPa and 330 °C. The dotted lines represent the prediction of kinetic model with a rate expression presented by Eq. 3.1.

build reaction models that accurately predict reaction rates under relevant conditions.

The Langmuir-Hinshelwood Hougen-Watson reaction scheme is a plausible alternative mechanism that can elucidate the NO oxidation over Pt catalysts. In this scheme (Scheme 2), both reactant molecules of NO and O_2 adsorb on Pt sites (*, steps 2a and 2b respectively). Adsorbed molecular oxygen undergoes dissociation both via a direct route (step 2c) and an assisted route (step 2d). The latter step prevails by formation of adsorbed NO_2 species. Adsorbed NO_2 species may further be formed via reaction between adsorbed NO and atomically adsorbed oxygen (step 2e), before desorbing in the final fast equilibrated step to form product dioxide (step 2f). Rate expression for the overall reaction in which different assumptions for the RDSs are presented in Table 3.

The different rate expressions from the two rival mechanisms are presented in Table 2 for the Eley-Rideal type and in Table 3 for the Langmuir-Hinshelwood Hougen Watson type mechanisms. For consistency throughout the derivation of these expressions, the following denotations have been adopted: k_{O2} or K_{O2} refers to the rate constant or equilibrium constant for molecular adsorption of O_2, k_O or K_O refers to the rate constant or equilibrium constant for direct surface dissociation of adsorption to form O, k_{NO} or K_{NO} refers to the rate constant or equilibrium constant for NO adsorption (strictly applicable in the LH type mechanism), k_1 or K_1 refers to the rate constant or the equilibrium constant for the "first" surface reaction involving NO (either in gas or adsorbed phase) and molecularly adsorbed oxygen, k_2 or K_2 denotes the rate constant or the equilibrium constant the "second" surface reaction involving NO (either in gas or adsorbed phase) and adsorbed atomic oxygen, and K_{NO2} represents the equilibrium constant for NO_2 desorption. L is the total number of sites. We separately fitted each of these rate expressions to the experimental rate data presented in Fig. 2 and Fig. 3. The reaction order plots provided in Figure S9 of the supporting information show that under the prevailing reaction conditions, the order for NO ranges from 1.83 to 2.05 whereas O_2 order ranges from 0.38 to 0.42.

Despite the suitability of the Eley-Rideal mechanism for predicting oxidation for low NO reactant pressure/ concentration, the observed reaction rates at high NO reactant pressures used in this work could not be described accurately by previously proposed schemes of the Eley-Rideal type. This implied that Pt catalyzed NO oxidation mechanism under these conditions strongly depends on the reactant pressures, i.e., the mechanism changes with increasing reactant pressure. The reaction mechanism search was performed by fitting each of these rate expressions to the reaction rate data in Fig. 2 and Fig. 3 to each of these derived rate expressions and the results are presented in section S7 of the supplementary information. The eventual choice of elementary steps presented in case 2.4a was the most possible reaction sequence with $R^2 = 0.996$ (the derivation shown in section S10 of the supplementary information). In the case 2.4a, the molecular adsorption of O_2 and adsorption of NO are fast quasi-equilibrated steps. The LH type surface reaction between adsorbed NO and molecularly adsorbed oxygen comprises the slowest kinetically relevant step in the sequence and its rate constant appears in the rate equation. The second surface reaction involving adsorbed NO and adsorbed atomic oxygen occurs at a rate higher than the first surface reaction step. The last step in the reaction, desorption of NO_2 occurs reversibly. Pt catalyzed NO oxidation is known to be strongly inhibited by ubiquitous NO_2 presence [10] because

(1a)	$O_2 + * \rightleftarrows O_2*$	Case 1.1
(1b)	$O_2* + * \rightleftarrows 2O*$	Case 1.2
(1c)	$NO + O_2* + * \rightleftarrows NO_2* + O*$	Case 1.3
(1d)	$NO + O* \rightleftarrows NO_2*$	Case 1.4
(1e)	$NO_2* \rightleftarrows NO_2 + *$	

Scheme 1. Proposed elementary steps for NO oxidation over Pt involving Eley-Rideal mechanism.

Table 2
Rate expressions for the overall reaction for different Eley-Rideal reaction mechanisms involving different RDSs.

Rate-determining step	Scheme 1 rate expressions
Case 1.1 $O_2 + *\rightarrow O_2*$	$r = k_{O_2}\cdot P_{O_2}\dfrac{1}{1+\dfrac{P_{NO_2}}{K_{NO_2}K_2P_{NO}}+\dfrac{1}{K_1K_2}\left(\dfrac{P_{NO_2}}{K_{NO_2}P_{NO}}\right)^2}$
Case 1.2 $O_2* + * \rightarrow 2O*$	$r = k_o\cdot K_{O_2}P_{O_2}\left(\dfrac{1}{1+K_{O_2}P_{O_2}+\dfrac{K_{O_2}K_{NO_2}K_1P_{NO}P_{O_2}}{P_{NO_2}}}\right)^2$
	$r = k_o\cdot K_{O_2}P_{O_2}\left(\dfrac{1}{1+K_{O_2}P_{O_2}+\dfrac{P_{NO_2}}{K_{NO_2}K_2P_{NO}}}\right)^2$
Case 1.3 $NO + O_2* + *\rightarrow$ NO_2*+O*	$r = k_1\cdot P_{NO}K_{O_2}P_{O_2}\left(\dfrac{1}{1+K_{O_2}P_{O_2}+\sqrt{K_OK_{O_2}P_{O_2}}}\right)^2$
	$r = k_1\cdot P_{NO}K_{O_2}P_{O_2}\left(\dfrac{1}{1+K_{O_2}P_{O_2}+\dfrac{P_{NO_2}}{K_{NO_2}K_2P_{NO}}}\right)^2$
Case 1.4 $NO + O* \rightarrow NO_2*$	$r = k_2\cdot P_{NO}\sqrt{K_{O_2}K_OP_{O_2}}\ \dfrac{1}{1+K_{O_2}P_{O_2}+\sqrt{K_OK_{O_2}P_{O_2}}}$
	$r = k_2\cdot P_{NO}{}^2\dfrac{K_1K_{NO_2}K_{O_2}P_{O_2}}{P_{NO_2}}\dfrac{1}{1+K_{O_2}P_{O_2}+\dfrac{K_1K_{NO_2}K_{O_2}P_{O_2}P_{NO}}{P_{NO_2}}}$

product readsorption is followed by surface dissociation of NO_2*. The most abundant surface intermediates are taken to be O_2*, O*, and *. As seen in section S7 of the supplementary information, schemes that incorporated NO* as one of the most abundant surface intermediates did not yield suitable fits to the experimentally observed data. The term in the denominator depicts the adsorption term with a power (2 in this case) corresponding to two adsorbed species involved in the rate-limiting step. The denominator also depicts the surface coverages of intermediate species, O_2* and O* relative to free sites. For these conditions, the predicted and observed rates were compared in a parity plot shown in Fig. 4 with the corresponding fitting constants shown in Table 4. The calculated values for the rate and equilibrium constants following experimental rate data regression with rate expression in Eq. 3.1 at three different temperature are presented in Table 4.

$$r = k_1\cdot K_{O_2}K_{NO}P_{NO}P_{O_2}\left(\frac{1}{1+K_{O_2}P_{O_2}+\frac{P_{NO_2}}{K_{NO_2}K_{NO}K_2P_{NO}}}\right)^2 \quad (3.1)$$

$$\begin{matrix} \vdots & \vdots & \vdots \\ [*] & [O_2*] & [O*] \end{matrix}$$

Fig. 5 shows the Arrhenius and Van't Hoff plots for the kinetic and equilibrium constants presented in Table 4 showing linear dependencies with slopes corresponding to enthalpies of adsorption and activation energies. The adsorption enthalpy for O_2 adsorption and NO adsorption steps are negative as expected from the invariably exothermic nature of adsorption processes. Comparing the equilibrium constants for O_2 and NO adsorption, it is clear that K_{eq} for O_2 is an order of magnitude higher than that of NO. Despres et al. [12] argues that the surface-adsorbate bond energy for Pt-O is greater than that of Pt-NO. The initial adsorption heats for NO and O_2 over Pt are 160 and 335 kJ mol^{-1} respectively [33] demonstrating the difference in the adsorption requirements on Pt of the two reactant molecules.

The activation energy for the LH reaction step (step 2d) is 24 kJ mol^{-1}. Similar values of E_A for the elementary NO oxidation surface reaction step have been reported in literature. Mean field kinetic models applied to an Eley-Rideal type reaction and gave estimated values of E_A of 35 [34] and 40 kJ mol^{-1} [35]. These values are relatively low for a surface reaction step and serve to signify the decreasing trend of E_A with increasing surface coverage of adsorbed reacting species. The overall activation energy of NO oxidation over Pt catalysts can vary between 80 – 120 kJ mol^{-1} depending on reaction conditions [11,31]. Values of the overall activation energy are also sensitive to differential concentration gradients across the catalyst bed. Mulla et al. demonstrated that significant concentration gradients of NO_2 within the catalyst bed result in differences in activation energy (E_A) ranging between 40–80 kJ/mol [10]. The overall E_A are much higher than the those of individual elementary surface reaction step. This big difference is because the overall E_A is a complex function of activation energies and reaction enthalpies of individual elementary steps constituting the overall reaction [36]. The treatment of such a relationship is beyond the scope of this work.

(2a)	$NO + * \rightleftarrows NO*$	Case 2.1
(2b)	$O_2 + * \rightleftarrows O_2*$	Case 2.2
(2c)	$O_2* + * \rightleftarrows 2O*$	Case 2.3
(2d)	$NO* + O_2* \rightleftarrows NO_2* + O*$	Case 2.4
(2e)	$NO* + O* \rightleftarrows NO_2*$	Case 2.5
(2f)	$NO_2* \rightleftarrows NO_2 + *$	

Scheme 2. Proposed elementary steps for NO oxidation over Pt involving the Langmuir Hinshelwood Hougen Watson mechanism.

Table 3
Rate expressions for the overall reaction for different LHHW reaction mechanisms involving different RDSs.

Rate-determining step	Scheme 2 Rate expressions
Case 2.1 $O_2 + * \rightarrow O_2*$	$r = k_{O_2} \cdot P_{O_2} \frac{1}{1 + \frac{P_{NO_2}}{K_{NO_2} K_2 K_{NO} P_{NO}} + \frac{1}{K_1 K_2} \left(\frac{P_{NO_2}}{K_{NO} K_{NO_2} P_{NO}} \right)^2}$
Case 2.2 $O_2* + * \rightarrow 2O*$	$r = k_2 K_1 P_{O_2} \left(\frac{1}{1 + K_{O_2} P_{O_2} + \frac{k_O K_{O_2} P_{O_2} + k_1 K_{O_2} K_{NO} P_{NO} P_{O_2} + k_{-2} K_{NO_2}{}^{-1} P_{NO_2}}{k_2 K_{NO} P_{NO} + k_{-1} K_{NO_2}{}^{-1} P_{NO_2}}} \right)^2$
Case 2.3 $NO + * \rightarrow NO*$	$r = k_{NO} \cdot P_{NO} \frac{1}{1 + K_{O_2} P_{O_2} + \sqrt{K_{O_2} K_O P_{O_2}}}$
Case 2.4 $NO* + O_2* \rightarrow NO_2* + O*$	$r = k_1 \cdot K_{O_2} K_{NO} P_{NO} P_{O_2} \left(\frac{1}{1 + K_{O_2} P_{O_2} + \frac{P_{NO_2}}{K_{NO_2} K_{NO} K_2 P_{NO}}} \right)^2$ $r = k_1 \cdot K_{O_2} K_O P_{NO} P_{O_2} \left(\frac{1}{1 + K_{O_2} P_{O_2} + \sqrt{K_{O_2} K_O P_{O_2}}} \right)^2$
Case 2.5 $NO* + O* \rightleftarrows NO_2*$	$r = k_2 \cdot K_{NO} P_{NO} \sqrt{K_{O_2} K_O P_{O_2}} \left(\frac{1}{1 + K_{O_2} P_{O_2} + \sqrt{K_{O_2} K_O P_{O_2}}} \right)^2$ $r = k_2 \cdot \frac{(K_{NO} P_{NO})^2 K_O K_1 P_{O_2}}{K_{NO_2}{}^{-1} P_{NO_2}} \left(\frac{1}{1 + K_{O_2} P_{O_2} + \frac{K_{NO_2} K_{O_2} K_{NO} K_1 P_{NO} P_{O_2}}{P_{NO_2}}} \right)^2$

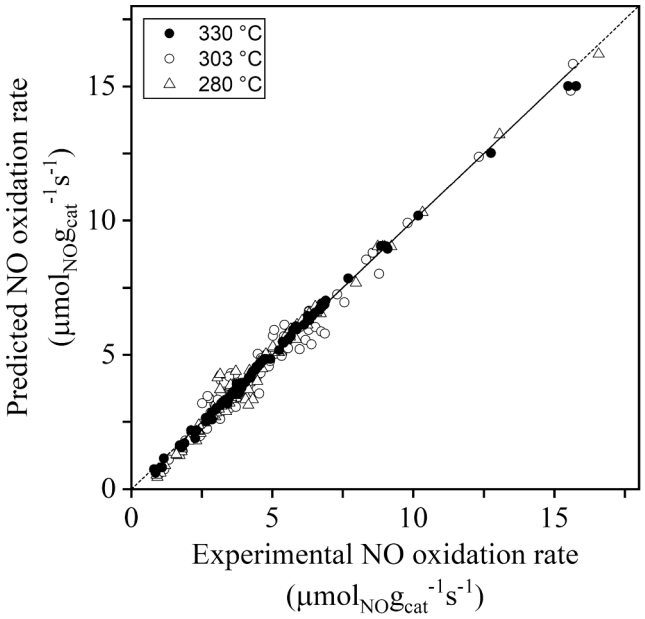

Fig. 4. Parity plot of experimental and predicted NO oxidation rate on Pt/SiO_2 at different test temperatures 330, 303, and 280 °C.

Conventional kinetic modeling provides a swift approach of shuffling through a large number of possibilities such that the implausible reaction models can be disregarded. The possibilities that remain after this elimination process can then be meticulously investigated using more powerful techniques. However, conventional kinetic modeling has two fundamental shortcomings. The rate expressions derived in this manner may not be sufficiently sensitive to the reaction rate data because different rate expressions (or models) based on varying assumption could suitably fit the measured rate data rather equally. This situation is encountered in this work with rate expressions in cases 1.3b and 2.4b since both share the assisted oxygen dissociation step as the rate determining step and provide good fits to the experimental data. Considering case 1.3b, it may be argued that the assisted oxygen dissociation step ($NO + O_2* + * \rightarrow NO_2* + O*$) is not a strictly Eley-Rideal type reaction because NO gas may occupy the available site before combining with O_2* in which situation, the step will correspond to a typical LH type surface reaction. Conversely, the strictly Eley-Rideal step $NO + O* \rightarrow NO_2*$ taken as the rate determining step did not provide a good fit to the data. Another drawback encountered using conventional kinetics approach is that the concentrations of surface intermediates involved in the reaction cannot be discerned from model calculations. Steady-state isotopic tracing using SSITKA, contrasting conventional kinetic modeling, provides a direct route for estimating not only the rate constants for each separate elementary reaction but also surface concentrations of intermediate species (i.e., surface abundancies). The next section presents the SSITKA in the investigation of the NO oxidation mechanism over Pt/SiO_2.

3.3. Steady-state isotopic transient kinetic analysis

3.3.1. Nitrogen path tracing during NO oxidation with ^{15}NO switch

To further investigate the oxidation reaction and obtain insights into the mechanism on Pt/SiO_2 we probed the nitrogen path during the

Table 4
Equilibrium and rate constants for NO oxidation over Pt/SiO_2 found by regressing experimental rate data with the rate expression Eq. 3.1.

T [K]	K_{O_2} [-]	K_{NO} [-]	k_1 [g(μmol·s)$^{-1}$]	K_2 [-]	K_{NO_2} [-]
553	4.525	$1.725 \cdot 10^{-1}$	2.107	$1.933 \cdot 10^{-3}$	$4.482 \cdot 10^{-1}$
576	3.959	$1.387 \cdot 10^{-1}$	2.854	$5.346 \cdot 10^{-3}$	$6.834 \cdot 10^{-1}$
603	3.248	$9.776 \cdot 10^{-2}$	3.265	$1.464 \cdot 10^{-2}$	$9.592 \cdot 10^{-1}$
ΔH_a or $\Delta E_{a,1}$ (kJ mol^{-1})	−18.40	−31.57	24.19	11.22	42.13

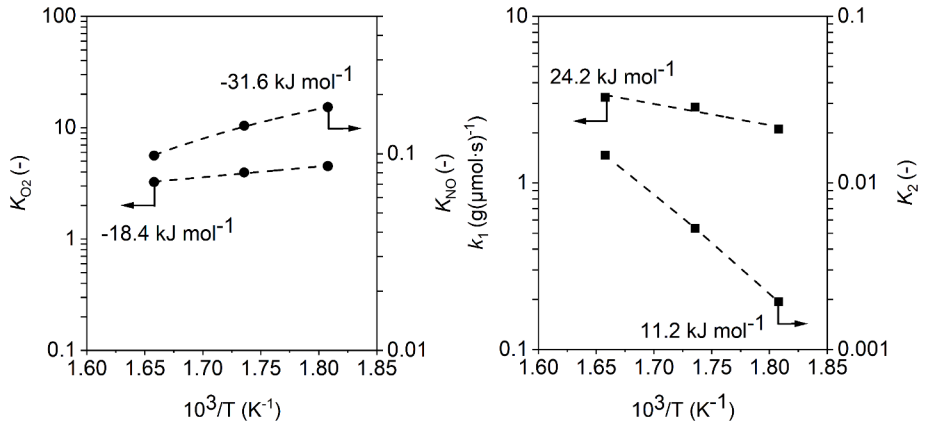

Fig. 5. Arrhenius and Van 't Hoff plots for K_{O2}, K_{NO}, k_1, and K_2 based on a probable rate expression in Eq. 3.1.

reaction by switching the reactant stream from $^{14}NO + O_2 + Ar$ // $^{15}NO + O_2 + Kr$ using the same standard reaction conditions as used in the temperature programmed reaction experiment; 5 mol% NO, 6 mol% O_2, 89 mol% Ar feed, 330 °C, 185 kPa, and 20 690 $Ncm^3\ g^{-1}h^{-1}$. Fig. 6 shows the time responses of $^{14}NO_2$ and $^{15}NO_2$ signals following a switch from $^{14}NO + O_2 + Ar$ // $^{15}NO + O_2 + Kr$. If the slight drift in the NO_2 signal were ignored, the steady state condition of the reaction regarding temperature, pressure, and thus effluent concentration of NO_2 was maintained. The signals were normalized with respect to the steady state NO_2 concentration to obtain the plot shown in Fig. 7.

Fig. 7 shows the normalized transient response for $^{15}NO_2$ and Kr following a switch from $^{14}NO + O_2 + Ar$ // $^{15}NO + O_2 + Kr$. For clarity, the $^{14}NO_2$ decay response is not shown here but presented in section S5 of the supplementary information. It is evident from Fig. 7 that the emergence of $^{15}NO_2$ transient response is delayed relative to the Kr response by some 6 s after the switch and assumes a characteristic curve shape reaching a new steady state within 54 s. The logarithmic plot of the $^{14}NO_2$ decay responses versus time at different temperatures are shown in Fig. 8. The trends of the logarithmic plots demonstrate a specific downward convexity of the isotopic response curves at different temperatures (with the logarithmic curves shifted in time for clarity). The downward convexity is indicative of a mechanism involving a buffer or parallel step [26,37].

The model fitting exercise reveals that many pathways fail to match with experimental data. These include a single NO* intermediate desorbing as NO_2 either reversibly (scheme A, fig. S24, SI) or irreversibly ((scheme B, fig. S25, SI), two adsorbed intermediates in series, one for

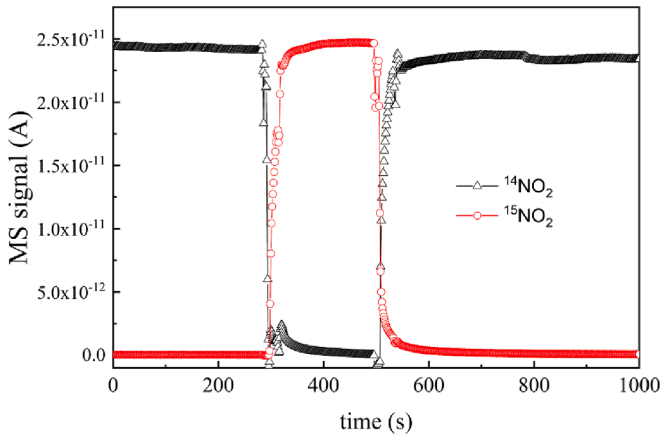

Fig. 6. Transient responses for the decay and emergence of $^{14}NO_2$ and $^{15}NO_2$ after switching from $^{14}NO/O_2/Ar$ to $^{15}NO/O_2/Kr$ (5/6/89 mol%) at 185 kPa, 20 690 $Ncm^3\ g^{-1}h^{-1}$ and 330 °C.

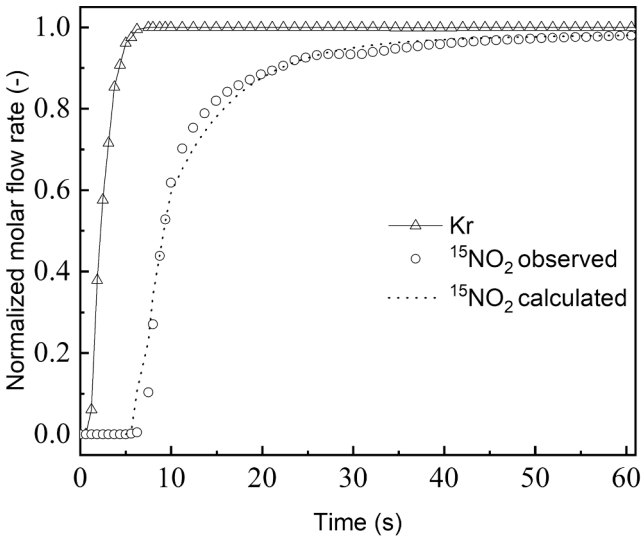

Fig. 7. Normalized responses for Kr and $^{15}NO_2$ concentrations following a switch from $^{14}NO/O_2/Ar$ to $^{15}NO/O_2/Kr$ (5/6/89 mol%) at 185 kPa and 330 °C. Model calculation is presented and described in section below.

adsorbed NO* and another for adsorbed NO_2* which irreversibly desorbs as NO_2 (scheme D, fig. S27, SI), the *NO_2 buffer species which exchanges with adsorbed *NO_2 alone without a *NO buffer pool (scheme G, fig. S30, SI), and the simultaneous formation of NO_2 from reversible oxidation of adsorbed *NO and irreversible oxidation of *NO buffer species to NO_2 (scheme I, fig. S32, SI), which also does not correspond to the observed transient kinetic responses.

3.3.2. *Oxygen path tracing during NO oxidation with $^{18}O_2$ switch*

The oxygen path during NO oxidation over Pt/SiO_2 was also investigated by switching the reactant stream from $NO+^{16}O_2 + Ar$ // $NO+^{18}O_2 + Kr$ using the same standard reaction conditions. After the switch, all possible product isotopologues were observed: $N^{16}O_2$, $N^{16}O^{18}O$, and $N^{18}O_2$. Fig. 9 and the accompanying normalized responses in Fig. 10 show the signal for the three species following the switch. $N^{16}O_2$ decays to a new steady state value higher than the new steady states for $N^{16}O^{18}O$ and $N^{18}O_2$ (i.e., the signal for $N^{16}O_2$ does not decay to zero but only reaches a new normalized steady state value of 0.6, shown in section S5 of the supplementary information). Transients of $N^{16}O_2$ fell slightly within 10 min after the switch and did not decay to zero. Similar isotopic decay trends to non-zero steady states involving $^{16}O_2$-$^{18}O_2$ isotopic switch have been observed elsewhere. Costa et al. observed the transient for $^{14}N_2O$ only reached 0.8 during an isotopic switch from NO/

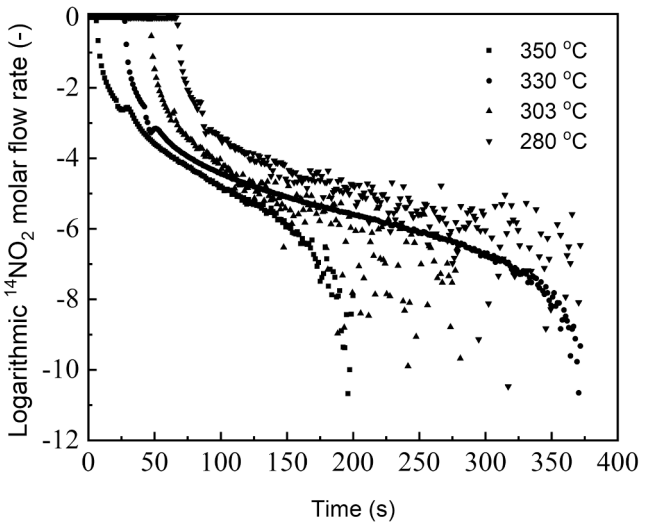

Fig. 8. Logarithmic plot of $^{14}NO_2$ normalized molar flow rate during a NO oxidation following a switch in NO with 2.2 wt% Pt/SiO_2 at different temperatures. The curves for 330, 303, and 280 °C are shifted slightly in time for separation of the curves and clarity.

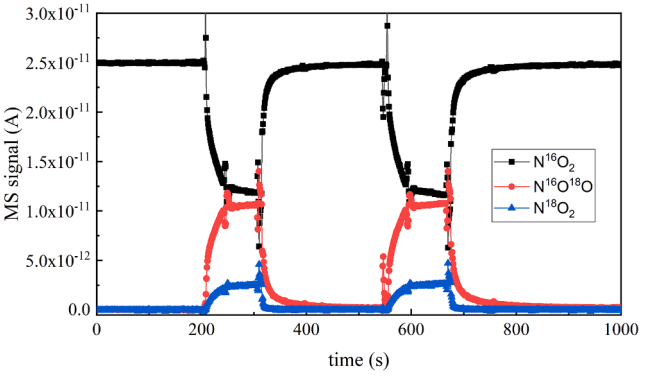

Fig. 9. Transient responses for the decay of $N^{16}O_2$ (black squares) and the emergence of $N^{16}O^{18}O$ (red circles), and $N^{18}O_2$ (blue triangles) after switching from $NO/^{16}O_2/Ar$ to $NO/^{18}O_2/Kr$. (5/6/89 mol%) at 185 kPa and 330 °C.

$H_2/^{16}O_2/Ar/He$ // $NO/H_2/^{18}O_2/He$ on investigating the SCR activity of over Pt/SiO_2 [23]. Similar non-zero decays have also been observed for the case of oxygen-exchange during CO oxidation over Au/TiO_2 [38] and other catalytic reactions [25]. The responses for $N^{16}O^{18}O$ and $N^{18}O_2$ increased slightly to new steady states. $N^{16}O^{18}O$ and $N^{18}O_2$ also do not grow to a normalized steady state of unity but only reach new steady states of 0.4 and 0.1, respectively. During a separate oxygen-only switch without NO, i.e., $^{16}O_2$ + Ar // $^{18}O_2$ + Kr, the unlabeled oxygen transients decayed to zero as expected. Taken together, these results indicate severe scrambling and exchange of oxygen from NO with that of labeled oxygen containing species. In Fig. 10 the curves for $N^{16}O^{18}O$ and $N^{18}O_2$ have a sigmoid shape with a considerable delay relative to the Kr curve. The S-shape is typical of a consecutive mechanism [26,37] for the surface catalyzed reaction.

The normalized transient data was kinetically analyzed and evaluated to obtain the mean surface residence time, kinetic rate constants, and the concentration of surface intermediates leading to formation of NO_2. We commenced the evaluation with simple models i.e., single pool, two pools in series, and two pools in parallel and one pool in series to prior parallel pools. None of these simplified model evaluations for a differential reactor would fit the data satisfactorily thus prompting the use of an integral reactor using the plug flow reactor (PFR) formalism that is mathematically described in Eq. 2.1-Eq. 2.4.

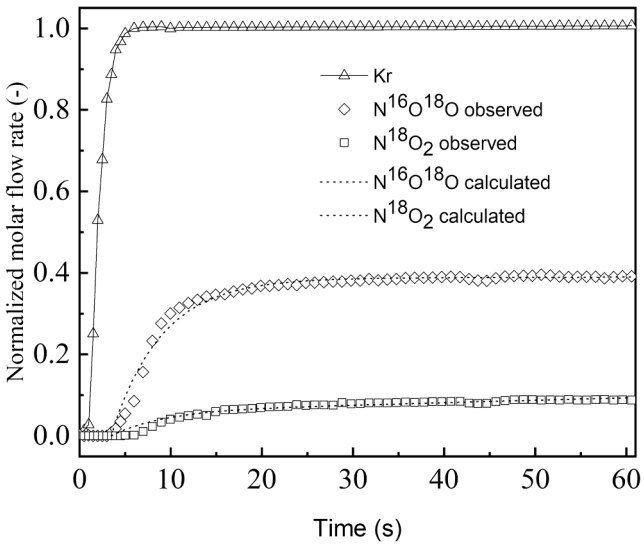

Fig. 10. Normalized transient responses for the decay of the emergence of $N^{16}O^{18}O$ and $N^{18}O_2$ after switching from $NO/^{16}O_2/Ar$ to $NO/^{18}O_2/Kr$ = 5/6/89 at 185 kPa and 330 °C.

3.3.3. *Reaction schemes for tracing transient responses*

The conversion of NO and O_2 after subtracting gas phase contribution from the total conversion were 19.5 % and 12.2 % respectively. Since these values were >10 %, a simplified kinetic evaluation of SSITKA data for differential flow reactors was not reliable. Therefore, an integral reactor model was applied to kinetically evaluate the NO oxidation under these degrees of conversion. The transient responses of isotopically labelled NO_2 were used to estimate the number of independent surface intermediates (pools), from which respective gas phase products are formed. The simplest model (one pool) was initially used to describe the experimental data. When this fitting was not satisfactory, the model complexity was increased by adding one or several additional pools.

Several alternative reaction sequences that represent the propagation of isotopic elements (i.e., ^{15}N and ^{18}O) into the product NO_2 are presented in sections S8 and S9 of the supplementary information. These sequences were expressed mathematically with the goal of describing the transient response shown in Fig. 7 and Fig. 10. For each of these schemes, two partial differential equations together with initial and boundary conditions (Eq. 2.1-Eq. 2.4) are used to capture the mass transfer rates by convection and dispersion along the reactor length as well as the reaction rate term. Upon integration, the solution of these equations was fitted to the experimentally observed transient data using statistical regression. A good model adequately fitting the experimental data for the nitrogen path was obtained with Scheme 3 and Scheme 4. These schemes were thus taken as the most probable sequences for tracing the path of nitrogen during NO oxidation over Pt/SiO_2. The depicted rate constants in these Scheme 3 and Scheme 4 include lumped kinetic parameters in which the rate constants k_i are multiplied by unknown concentration of adsorbed species or concentration of free sites. The use of lumped constants enables the determination of unknown

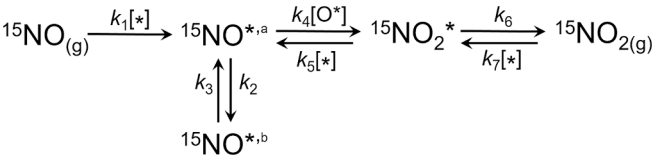

Scheme 3. Proposed reaction path for nitrogen during NO oxidation over Pt/SiO_2 with two pools of intermediates in series traced using ^{15}NO reactant.

$$^{15}NO_{(g)} \xrightarrow{k_1[*]} {}^{15}NO^* \xrightarrow{k_2[O^*]} {}^{15}NO_2{}^* \underset{k_4[*]}{\overset{k_3}{\rightleftharpoons}} {}^{15}NO_{2(g)}$$

Scheme 4. Proposed reaction path for nitrogen during NO oxidation over Pt/SiO_2 with pools of intermediates in series with an additional buffer step for adsorbed NO, traced using ^{15}NO reactant.

parameters such as concentration of free sites and the surface concentration of adsorbed species during the reaction.

Scheme 3 shows a possible pathway for nitrogen having two pools of surface intermediates during NO oxidation; nitric oxide adsorbs on an adsorption site via an intermediate of NO. The latter undergoes reaction with adsorbed oxygen to form higher oxide NO_2 that subsequently desorbs to form NO_2. The desorption step is accompanied with a product readsorption step. Another plausible nitrogen path is shown in Scheme 4 involves three pools of surface intermediates. NO reversibly adsorbs onto the surface to form adsorbed NO denoted as $NO^{*,a}$. This intermediate is in exchange with a second pool of NO* denoted as $NO^{*,b}$. Although $NO^{*,b}$ may not directly participate in the reaction, it acts as a buffer, replenishing $NO^{*,a}$, an adsorbed intermediate directly involved in the surface reaction with activated oxygen species. In the final step, NO_2* reversibly desorbs from the surface forming gas phase NO_2. Notably, the latter scheme demonstrates a slightly better coefficient of correlation ($R^2 = 0.992$) compared to the calculated value for Scheme 3 ($R^2 = 0.986$). Generally, the coefficient of correlation obtained by fitting provides the first estimate of the validity of a model and thus the choice of the most plausible reaction route could not be made solely based on these values. A further test was required to determine which of these models described the transient data better.

To discriminate between Scheme 3 and Scheme 4 we employed an approach previously used by Gayubo et al. [39], that determines the statistical significance of each model. A comparison was made between the ratio of the *variance* due to the coefficient of correlation, S_f^2 to the variance due to the experimental error S_e^2. For a good fit, this ratio ought to be low and the acceptance criteria can be defined so that the ratio must be less than the F-value (i.e., F-test criteria). The F-value can be determined as the inverse cumulative distribution function [40,41]. The results from the fitting and the model discrimination criteria for nitrogen path between these two schemes are shown in Table 5.

Of the possible alternative oxygen path schemes (presented in section S9 of the supplementary information), one path shown in Scheme 5 provided a good fit to the experimental data for the oxygen tracing for NO oxidation over Pt/SiO_2 under the prevailing conditions. Scheme 5 provides for the following steps: $^{18}O_2$ reversibly adsorbs on the surface of the Pt/SiO_2 to form molecularly adsorbed oxygen ($^{18}O_2$*). Adsorbed molecular oxygen dissociates directly in a subsequent step forming atomically adsorbed oxygen. This model assumes the participation of

Table 5
Kinetic parameters of the nitrogen reaction path from Scheme 3 and Scheme 4 obtained by fitting experimental transient data.

Kinetic parameters for modeled nitrogen pathway			
τ (s)	11.73		
N_{NO2} (μ|mol/g_{cat})	$3.65\cdot10^{-4}$		
Scheme 3 rate constants		Scheme 4 rate constants	
k_1[*] /μmol(g.s.kPa)$^{-1}$	21.8	k_1[*] /μmol(g.s.kPa)$^{-1}$	2.4
k_2[O*] /m^3(g.s)$^{-1}$	$3.7\cdot10^{-1}$	k_2 / –	$4.8\cdot10^{-2}$
k_3/m^3(g.s)$^{-1}$	$1.5\cdot10^{-1}$	k_3 / –	$2.4\cdot10^{-4}$
k_4[*]/m^3(g.s)$^{-1}$	$6.9\cdot10^{-4}$	k_4[O*] / m^3(g.s)$^{-1}$	$2.8\cdot10^{-3}$
		k_5[*] / m^3(g.s)$^{-1}$	$5.8\cdot10^{-2}$
		k_6 /m^3(g.s)$^{-1}$	$8.3\cdot10^{-1}$
		k_7[*] / μmol(g.s.kPa)$^{-1}$	$7.5\cdot10^{-4}$
S_f^2/S_e^2	0.1136	S_f^2/S_e^2	0.0084
$F_{0.05}(\nu_e,\nu_f)$	0.1047	$F_{0.05}(\nu_e,\nu_f)$	0.0540
Criteria	Reject	Criteria	Accept

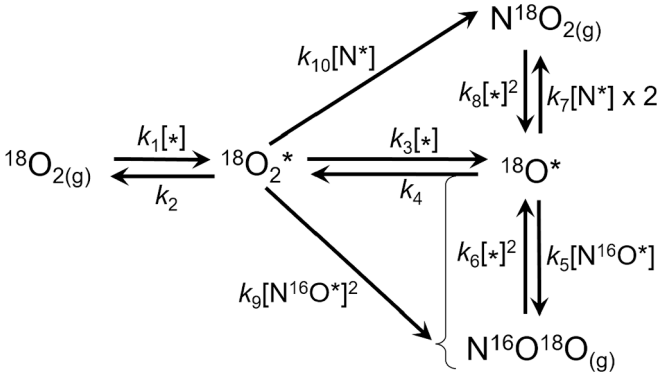

Scheme 5. Proposed reaction path for nitrogen during NO oxidation over Pt/SiO_2 with two pools of intermediates in series traced using ^{15}NO.

both these oxygen species (O_2* and O*) towards NO_2 formation and these oxygen species react at varying rates as suggested in the kinetic inquiry (section 3.2.1). Throughout the sequence, the slowest of steps (lowest k_i) is the direct dissociation of $^{18}O_2$* to form O*. The fastest step (highest k_i) in the sequence involves the adsorption of oxygen; shown with an adsorption rate constant; k_1[*]. From Fig. 10, the ratio of the normalized steady-state responses for $N^{16}O^{18}O$ to $N^{18}O_2$ is 4:1. Formation of NO_2 from atomic oxygen occurs at a rate slower than NO_2 formation from $^{18}O_2$. Respective values of kinetic parameters determined by data fitting to the oxygen isotopic transient are presented in Table 6. From this table, it is evident that the rate constants for the steps involving NO_2 formation from molecularly adsorbed oxygen i.e., $K_9[N^{16}O^*]^2$ and $K_{10}[N^*]$ are at least an order of magnitude higher than those similar steps involving dissociated oxygen, i.e., $k_5[N^{16}O^*]$, $k_6[^*]$, $k_7[N^*]$, and $k_8[^*]$. It is important to remember that these kinetic parameters are lumped constants and contain unknown values of intermediates and free sites concentration. Nevertheless, these results serve to show that formation NO_2 from O_2* and O* occur at very different rates. This aspect of the surface reaction supports earlier conclusions reached in section 3.2.1.

As seen from Fig. 9 the signal $N^{16}O^{18}O$ molar flow rate is more than twice as much as $N^{18}O_2$ molar flow rate. The level of formation of $N^{16}O^{18}O$ and $N^{18}O_2$ product species is an indicator of the rates of participation of adsorbed oxygen species. This result signifies limited formation of $N^{18}O_2$ potentially from molecularly adsorbed isotopic oxygen ($^{18}O_2$*) and a concomitant (considerable) formation of $N^{16}O^{18}O$ possibly from atomically adsorbed labeled ^{18}O*. This supports the conclusion drawn from the scheme from the kinetic inquiry: the limited formation of $N^{18}O_2$ comports with a slow step (NO*+O_2*→NO_2*+O*) while formation of $N^{16}O^{18}O$ (from step NO*+O*→NO_2*) occurs at a relatively faster rate than the previous step. It is difficult to directly compare rates of these two reaction steps above due to the challenges of estimating surface concentration (abundancy) of adsorbed NO. However, the kinetic parameter from the oxygen switch presented and

Table 6
Kinetic parameters of the oxygen reaction path for reaction scheme 5 obtained by fitting transient data.

Scheme 5 rate constants	
k_1[*]/μmol(g.s.kPa)$^{-1}$	6.8
k_2 /m^3(g.s)$^{-1}$	$5.5\cdot10^{-3}$
k_3[*] /m^3(g.s)$^{-1}$	$1.0\cdot10^{-4}$
k_4 /m^6(μmol.g.s)$^{-1}$	$1.0\cdot10^{-5}$
k_5[$N^{16}O^*$] /m^3(g.s)$^{-1}$	$1.8\cdot10^{-4}$
k_6[*]^2 /μmol(g.s.kPa)$^{-1}$	$5.8\cdot10^{-4}$
k_7[N*] /m^3(g.s)$^{-1}$	$9.5\cdot10^{-4}$
k_8[*]^2 /μmol(g.s.kPa)$^{-1}$	$3.9\cdot10^{-4}$
k_9[$N^{16}O^*$] /m^3(g.s)$^{-1}$	$1.6\cdot10^{-1}$
k_{10}[N*] /m^3(g.s)$^{-1}$	$1.8\cdot10^{-2}$

calculated as shown in Scheme 5 and Table 6 clearly indicates that possibility of de-lumping these rate constants for a direct comparison between the relative rates. We acknowledge the fact that more future experimentations can provide more information for directly comparing rates of these elementary steps.

4. Conclusion

This study provides a plausible reaction mechanism for NO oxidation prevailing under conditions of high concentration and high temperature using both conventional kinetic inquiry and intrinsic isotope tracing. Using the two modeling approaches, the Langmuir-Hinshelwood type reaction is identified as more probable to an alternative Eley-Rideal mechanism. A Langmuir - Hinshelwood surface reaction between adsorbed NO and molecularly adsorbed O_2 with an activation barrier of 24 kJ mol^{-1} is identified under the prevailing reaction conditions of NO oxidation over 2.2 wt% Pt/SiO_2. These insights can be a starting point in the understanding Pt catalyzed NO oxidation under these conditions of high NO reactant concentration, spawning further studies.

The adsorption of NO occurs simultaneously with O_2 adsorption onto the same type of sites. Adsorbed NO occupies two pools of intermediate species, one pool acting as a buffer to the main pool whereas molecularly adsorbed O_2 and chemisorbed O each occupy one pool leading to the formation of NO_2. However, the equilibrium constant for O_2 adsorption was found to be an order of magnitude higher than that of NO. This signifies that the Pt surface is far more dominated by molecularly adsorbed O_2 than NO*. However, the reaction between these two surface adsorbed species was found to be the slowest in the reaction sequence. Direct (unassisted) dissociation pathway for oxygen plays almost no part in NO oxidation and this insight is supported by two sets of evidence. 1) the kinetic model considering direct dissociation being a fast quasi-equilibrated or RDS did not provide satisfactory fit to the data, and 2) $^{18}O_2$ pathway model showed that the forward and reverse lumped rate constant (k_3[*] and k_4 respectively from Scheme 5) are indeed small. Surface reaction leading to formation of adsorbed NO_2 occurs via two disparate but consecutive paths, one directly leading to another. The first kinetically-significant reaction involves surface combination of NO* and ubiquitous O_2* to form NO_2. This reaction also serves as a source of O* as an assisted dissociation pathway. Adsorbed NO reacts with O* in a relatively fast step and the desorption of NO_2 is a fast equilibrated process in agreement with product inhibition for NO oxidation.

CRediT authorship contribution statement

Moses Mawanga: Data curation, Formal analysis, Investigation, Visualization, Writing – original draft, Writing – review & editing. **Jia Yang:** Data curation, Formal analysis, Investigation, Methodology, Supervision, Writing – original draft, Writing – review & editing, Conceptualization. **Edd Anders Blekkan:** Supervision, Project administration, Investigation, Funding acquisition, Formal analysis, Conceptualization, Writing – review & editing.

Declaration of competing interest

The authors declare the following financial interests/personal relationships which may be considered as potential competing interests: Edd Anders Blekkan reports financial support was provided by Research Council of Norway. If there are other authors, they declare that they have no known competing financial interests or personal relationships that could have appeared to influence the work reported in this paper.

Data availability

Data will be made available on request.

Acknowledgement

The authors greatly acknowledge the financial support from the center of industrial Catalysis Science and Innovation (iCSI), a center for Research-based Innovation funded by the Research Council of Norway under Grant number 237922.

Appendix A. Supplementary material

Supplementary material to this article can be found online at https://doi.org/10.1016/j.jcat.2024.115483.

References

[1] J. Pérez-Ramírez, F. Kapteijn, K. Schöffel, J.A. Moulijn, Formation and control of N_2O in nitric acid production: where do we stand today? Appl. Catal. B Environ. 44 (2003) 117–151, https://doi.org/10.1016/S0926-3373(03)00026-2.
[2] A.C.A. De Vooys, G.L. Beltramo, B. Van Riet, J.A.R. Van Veen, M.T.M. Koper, Mechanisms of electrochemical reduction and oxidation of nitric oxide, Electrochim. Acta. 49 (2004) 1307–1314, https://doi.org/10.1016/j.electacta.2003.07.020.
[3] H. Wiesenberger, State-Of-The-Art for the Production of Nitric Acid with regard to the IPPC Directive, Wien, 2001.
[4] H. Tsukahara, T. Ishida, M. Mayumi, Gas-phase oxidation of nitric oxide: chemical kinetics and rate constant, nitric oxide -, Nitric oxide 3 (1999) 191–198, https://doi.org/10.1006/niox.1999.0232.
[5] C.A. Grande, K.A. Andreassen, J.H. Cavka, D. Waller, O.A. Lorentsen, H. Øien, H. J. Zander, S. Poulston, S. García, D. Modeshia, Process intensification in nitric acid plants by catalytic oxidation of nitric oxide, Ind. Eng. Chem. Res. 57 (2018) 10180–10186, https://doi.org/10.1021/acs.iecr.8b01483.
[6] A.u.R. Salman, B.C. Enger, X. Auvray, R. Lødeng, M. Menon, D. Waller, M. Rønning, Catalytic oxidation of NO to NO_2 for nitric acid production over a Pt/Al_2O_3 catalyst, Appl. Catal. A Gen. 564 (2018) 142–146, https://doi.org/10.1016/j.apcata.2018.07.019.
[7] J. Gopakumar, P.M. Benum, I.H. Svenum, B.C. Enger, D. Waller, M. Rønning, Redox transformations of ru catalyst during NO oxidation at industrial nitric acid production conditions, Chem. Eng. J. 475 (2023) 146406, https://doi.org/10.1016/J.CEJ.2023.146406.
[8] J. Gopakumar, S. Vold, B. Christian Enger, D. Waller, P. Erik Vullum, M. Rønning, Catalytic oxidation of NO to NO_2 for industrial nitric acid production using ag-promoted MnO_2/ZrO_2 catalysts, Catal. Sci. Technol. 13 (2023) 2783, https://doi.org/10.1039/d2cy02178a.
[9] A.D. Smeltz, R.B. Getman, W.F. Schneider, F.H. Ribeiro, Coupled theoretical and experimental analysis of surface coverage effects in Pt-catalyzed NO and O_2 reaction to NO_2 on Pt(111), Catal. Today. 136 (2008) 84–92, https://doi.org/10.1016/j.cattod.2007.12.139.
[10] S.S. Mulla, N. Chen, W.N. Delgass, W.S. Epling, F.H. Ribeiro, NO_2 inhibits the catalytic reaction of NO and O_2 over Pt, Catal. Letters. 100 (2005) 267–270, https://doi.org/10.1007/s10562-004-3466-1.
[11] B.M. Weiss, E. Iglesia, NO oxidation catalysis on Pt clusters: Elementary steps, structural requirements, and synergistic effects of NO_2 adsorption sites, J. Phys. Chem. C. 113 (2009) 13331–13340, https://doi.org/10.1021/jp902209f.
[12] J. Després, M. Elsener, M. Koebel, O. Kröcher, B. Schnyder, A. Wokaun, Catalytic oxidation of nitrogen monoxide over Pt/SiO_2, Appl. Catal. B Environ. 50 (2004) 73–82, https://doi.org/10.1016/j.apcatb.2003.12.020.
[13] L. Olsson, H. Persson, E. Fridell, M. Skoglundh, B. Andersson, A kinetic study of NO oxidation and NOx storage on Pt/Al_2O_3 and $Pt/BaO/Al_2O_3$, J. Phys. Chem. B. 105 (2001) 6895–6906, https://doi.org/10.1021/jp010324p.
[14] B. Choi, K. Lee, G. Son, Review of recent after-treatment Technologies for de-NO_x process in diesel engines, Int. J. Automot. Technol. 216 (21) (2020) 1597–1618, https://doi.org/10.1007/S12239-020-0150-4.
[15] B.M. Weiss, N. Artioli, E. Iglesia, Catalytic NO oxidation pathways and redox cycles on dispersed oxides of rhodium and cobalt, ChemCatChem. 4 (2012) 1397–1404, https://doi.org/10.1002/cctc.201200050.
[16] M. Iwasaki, E. Iglesia, Mechanistic assessments of NO oxidation turnover rates and active site densities on WO_3-promoted CeO_2 catalysts, J. Catal. 342 (2016) 84–97, https://doi.org/10.1016/j.jcat.2016.07.011.
[17] S.L. Shannon, J.G. Goodwin, Characterization of catalytic Surfaces by isotopic-transient kinetics during steady-state reaction, Chem. Rev. 95 (1995) 677–695, https://doi.org/10.1021/cr00035a011.
[18] C. Mirodatos, Use of isotopic transient kinetics in heterogeneous catalysis, Catal. Today. 9 (1991) 83–95, https://doi.org/10.1016/0920-5861(91)85011-V.
[19] C. Ledesma, J. Yang, D. Chen, A. Holmen, Recent approaches in mechanistic and kinetic studies of catalytic reactions using SSITKA technique, ACS Catal. 4 (2014) 4527–4547, https://doi.org/10.1021/cs501264f.
[20] P. Janssens, J. Poissonnier, A. Chakkingal, R. Bos, J.W. Thybaut, Recent advances in the use of steady-state isotopic transient kinetic analysis data in (micro)kinetic modeling for catalyst and process design, Catal. Commun. 179 (2023) 106688, https://doi.org/10.1016/j.catcom.2023.106688.
[21] A. Holmen, J. Yang, D. Chen, Steady-state isotopic transient kinetic analysis (SSITKA), in: Springer Handbooks, Springer Science and Business Media

Deutschland GmbH, 2023, pp. 935–965, https://doi.org/10.1007/978-3-031-07125-6_41.
[22] J. Yang, Y. Qi, J. Zhu, Y.A. Zhu, D. Chen, A. Holmen, Reaction mechanism of CO activation and methane formation on co fischer-tropsch catalyst: a combined DFT, transient, and steady-state kinetic modeling, J. Catal. 308 (2013) 37–49, https://doi.org/10.1016/J.JCAT.2013.05.018.
[23] C.N. Costa, A.M. Efstathiou, Transient isotopic kinetic study of the NO/H_2/O_2 (lean de-NO_x) reaction on Pt/SiO_2 and Pt/La-Ce-Mn-O catalysts, J. Phys. Chem. B. 108 (2004) 2620–2630.
[24] R. Burch, M.D. Coleman, An investigation of promoter effects in the reduction of NO by H_2 under lean-burn conditions, J. Catal. 208 (2002) 435–447, https://doi.org/10.1006/JCAT.2002.3596.
[25] S. Reining, E.V. Kondratenko, N.V. Kalevaru, A. Martin, Steady-state and transient kinetic studies of the acetoxylation of toluene over pd-Sb/TiO_2, ACS Catal. 6 (2016) 4621–4629, https://doi.org/10.1021/ACSCATAL.6B00646/ASSET/IMAGES/LARGE/CS-2016-00646R_0009.JPEG.
[26] E.M. Sadovskaya, D. Bulushev, B.S. Bal'zhinimaev, Dynamics of isotopic label transfer in catalytic reactions, Kinet. Catal. 40 (1999) 54–61.
[27] E. Xue, K. Seshan, J.R.H. Ross, Roles of supports, Pt loading and Pt dispersion in the oxidation of NO to NO_2 and of SO_2 to SO_3, Appl. Catal. B Environ. 11 (1996) 65–79, https://doi.org/10.1016/S0926-3373(96)00034-3.
[28] R.J. Berger, F. Kapteijn, J.A.J. Moulijn, G.B. Marin, J. De Wilde, M. Olea, D. Chen, A. Holmen, L. Lietti, E. Tronconi, Y. Schuurman, E. Tronconi, Y. Schuurman, Dynamic methods for catalytic kinetics, Appl. Catal. A Gen. 342 (2008) 3–28, https://doi.org/10.1016/j.apcata.2008.03.020.
[29] S.C. Van Der Linde, T.A. Nijhuis, F.H.M. Dekker, F. Kapteijn, J.A. Moulijn, Mathematical treatment of transient kinetic data: combination of parameter estimation with solving the related partial differential equations, Appl. Catal. A Gen. 151 (1997) 27–57, https://doi.org/10.1016/S0926-860X(96)00260-8.
[30] B.M. Weiss, E. Iglesia, Mechanism and site requirements for NO oxidation on Pd catalysts, J. Catal. 272 (2010) 74–81, https://doi.org/10.1016/j.jcat.2010.03.010.
[31] S.S. Mulla, N. Chen, L. Cumaranatunge, G.E. Blau, D.Y. Zemlyanov, W.N. Delgass, W.S. Epling, F.H. Ribeiro, Reaction of NO and O_2 to NO_2 on Pt: kinetics and catalyst deactivation, J. Catal. 241 (2006) 389–399, https://doi.org/10.1016/j.jcat.2006.05.016.
[32] A. Groß, A. Eichler, J. Hafner, M.J. Mehl, D.A. Papaconstantopoulos, Unified picture of the molecular adsorption process: O_2/Pt(1 1 1), Surf. Sci. 539 (2003) L542–L548, https://doi.org/10.1016/S0039-6028(03)00791-X.
[33] C.E. Wartnaby, A. Stuck, Y.Y. Yeo, D.A. King, Microcalorimetric heats of adsorption for CO, NO, and oxygen on Pt{110}, J. Phys. Chem. 100 (1996) 12483–12488, https://doi.org/10.1021/JP953624D/ASSET/IMAGES/LARGE/JP953624DF00003.JPEG.
[34] M. Crocoll, S. Kureti, W. Weisweiler, Mean field modeling of NO oxidation over Pt/Al_2O_3 catalyst under oxygen-rich conditions, J. Catal. 229 (2005) 480–489, https://doi.org/10.1016/j.jcat.2004.11.029.
[35] L. Olsson, B. Westerberg, H. Persson, E. Fridell, M. Skoglundh, B. Andersson, A kinetic study of oxygen adsorption/desorption and NO oxidation over Pt/Al_2O_3 catalysts, J. Phys. Chem. B. 103 (1999) 10433–10439, https://doi.org/10.1021/jp9918757.
[36] J.A. Moulijn, P. van Leeuwen, R.A. van Santen, Chemical kinetics of catalyzed reactions, in: Stud. Surf. Sci. Catal., Elsevier, 1993: pp. 69–86. https://doi.org/10.1016/S0167-2991(99)80006-8.
[37] B.S. Bal'zhinimaev, E.M. Sadovskaya, A.P. Suknev, Transient isotopic kinetics study to investigate reaction mechanisms, Chem. Eng. J. 154 (2009) 2–8, https://doi.org/10.1016/j.cej.2009.04.035.
[38] J.T. Calla, R.J. Davis, Oxygen-exchange reactions during CO oxidation over titania- and alumina-supported Au nanoparticles, J. Catal. 241 (2006) 407–416, https://doi.org/10.1016/j.jcat.2006.05.017.
[39] A.G. Gayubo, A. Alonso, B. Valle, A.T. Aguayo, M. Olazar, J. Bilbao, Kinetic modelling for the transformation of bioethanol into olefins on a hydrothermally stable Ni–HZSM-5 catalyst considering the deactivation by coke, Chem. Eng. J. 167 (2011) 262–277, https://doi.org/10.1016/J.CEJ.2010.12.058.
[40] J.F. Harper, Precise calculation of the cumulative distribution function and its inverse function for fisher's F and student's t tests, Comput. Methods Programs Biomed. 21 (1985) 127–129, https://doi.org/10.1016/0169-2607(85)90073-2.
[41] D. Buckwitz, H.G. Holzhutter, A new method to discriminate between enzyme-kinetic models, Comput. Math. Applic. 20 (1990) 117–126.